Available online at www.sciencedirect.com

ScienceDirect

Acta Materialia 73 (2014) 149–166

Acta MATERIALIA

www.elsevier.com/locate/actamat

Extended defects, ideal strength and actual strengths of finite-sized metallic glasses

Pengyang Zhao [a], Ju Li [b,*], Yunzhi Wang [a,*]

[a] Department of Materials Science and Engineering, The Ohio State University, Columbus, OH 43210, USA

[b] Department of Nuclear Science and Engineering, Department of Materials Science and Engineering, Massachusetts Institute of Technology, Cambridge, MA 02139, USA

Received 16 January 2014; received in revised form 30 March 2014; accepted 31 March 2014

Abstract

Initial condition dependence is the key to understanding the difference between ideal strength and actual strength of both crystalline and amorphous materials. Besides intrinsic structural heterogeneities in metallic glasses (MGs), a class of "extended defects" based on the "connected atomistic free volume" (CAFV) is proposed to define the microstructure (initial condition), which is crucial to understanding the strength. To explore these concepts and theories, deformation of finite-sized MG samples with different populations of pre-existing extended defects (damages) are simulated using a nanometer-scale shear transformation zone (STZ) model based on microelasticity and the kinetic Monte Carlo method. A "smaller is stronger" effect on the peak stress of simulated true stress–strain curves is seen in samples with pre-existing damage introduced as post-activated STZ clusters. Samples with "chemically contaminated" surface STZs also exhibit a size effect on the peak stress, and depending on whether the surface STZs are softer or harder than the bulk STZs, smaller can be either weaker or stronger.

Keywords: Metallic glass; Yield strength; Size effect; Shear band; Computer simulations

1. Introduction

It was the striking difference between Frenkel's prediction of ideal shear strength and the experimentally measured yield strength that inspired Orowan, Polanyi and Taylor to predict the presence of dislocations in real crystals [1]. This has led to significant advances in physical metallurgy based on controlling dislocation/grain boundary populations and activities in alloys. Realizing that the strength of a solid depends on its current microstructure, which is a function of past processing and service history, has revolutionized the way of thinking in materials science. To predict the mechanical behavior of a material, knowing just the crystal structure and chemical composition, is usually not sufficient. It is equally vital to know the initial condition (IC) of the defect populations such as the grain size distribution and dislocation density. For instance, by producing crystals with fewer and fewer pre-existing dislocations, their low-temperature local strength will eventually converge to Frenkel's theoretical prediction of $\sigma_{\text{ideal}} \sim 0.1G$ where G is the shear modulus [2].

This microstructure dependence of materials properties is also true in computer simulations. For instance, in order to simulate plastic yielding of a crystalline metal by ramping up the stress of a simulation supercell in a large-scale molecular dynamics (MD) simulation, one needs an IC for the atomic positions $\mathbf{x}^{3N}$, where N is the number of atoms. While it is very easy (and therefore tempting in

* Corresponding authors.

E-mail addresses: zhao.247@osu.edu (P. Zhao), liju@mit.edu (J. Li), wang.363@osu.edu (Y. Wang).

http://dx.doi.org/10.1016/j.actamat.2014.03.068

1359-6454/

practice) to build a perfect single-crystal supercell as IC_A, it takes significantly more effort to add a dislocation loop to this supercell (IC_B), as one needs to arrange the atoms properly according to dislocation theory and anisotropic elasticity. In the subsequent MD simulation these two ICs would give very different results, involving different physics. With IC_A, one will get the impression from the simulation that plastic yielding occurs near the ideal strength σ_{ideal} as Frenkel predicted, and the expressed physics is homogeneous dislocation nucleation. With IC_B, the obtained yield strength may be 10- to 1000-fold smaller than σ_{ideal}, depending on the size of the initial dislocation loop that one puts in, and the expressed physics would be dislocation line tension and perhaps Peierls stress of the dislocation core, and dislocation multiplication, intersection and junction formation. Thus, the same MD simulation code and the same boundary conditions (stress ramp-up at the same temperature, with the same periodic boundary condition) will paint quite different physical pictures. The famous experimentalists' mantra "microstructure determines properties" simply translates to expecting large "initial condition sensitivity" in computer simulations of strength, ductility and other mechanical properties. The fundamental cause for the above is that defects such as dislocations do not have a thermal equilibrium distribution: they exist only in strongly driven, out-of-thermal-equilibrium dissipative situations, and thus are strongly history dependent.

Our adventure with simulating and understanding metallic glass (MG) strength is likely to follow a similar route, even though identifying/describing the "microstructure" of a glass is still a semantically complex and experimentally unsolved problem. We use words such as "shear bands" to describe what little we can see with microscopy and spectroscopy of these extended defects in MGs, but we do not yet have experimental characterization techniques approaching the precision and resolution of "g-dot-b" analysis and direct STEM-EELS imaging of dislocation core for crystals. Temporally extended flow defects emerge in stressed MGs in a totally unstable manner (explosive growth in a very short time), at least in bulk samples, further hampering stable experimental observations. As a flip-side to the experimental difficulties of "microstructural characterization" in MGs, in simulations the aforementioned IC sensitivity issue is quite often simply ignored. The present work aims to explore this initial condition sensitivity in MG numerically by properly defining "extended defects", "microstructure" and "ideal strength" for glasses, and to show that the strength of a glass sample is really an IC- and size-dependent quantity, just like in crystals.

So far, experiments on various bulk metallic glasses (BMGs) have revealed a peak shear stress limit of $\sigma_{peak}^{BMG} \approx 0.036G$ at $T = 0$ K [3]. But this may not be the "ideal strength" σ_{ideal} of MG, if we heed the story of crystals. Obviously $\sim 0.036G$ is still ~ 3 times less than $\sim 0.1G$, the usual ideal shear strength of simple metallic crystals without surfaces [2]. For reference, σ_{ideal} of a crystal is defined at temperature $T = 0$ K as the maximum stress that a perfect crystal without any defect—even surfaces—can sustain indefinitely without losing homogeneity of the lattice or undergoing phase transformation. (Such perfect crystal configurations without surfaces exist in computer simulations only, under the periodic boundary condition (PBC), also known as the Born–von Karman boundary condition.) However, should a MG also have a similar normalized "ideal strength" akin to that of simple crystals? Even more fundamentally, should MGs have an "ideal strength"? And what would be the meaning of such a concept atomistically for a material that has intrinsic (as well as possible extrinsic) heterogeneities? This is the first conceptual question that this paper aims to answer.

If one takes a pragmatic approach, and defines σ_{ideal} as the lowest "upper bound" to the measurable strength of a MG at $T = 0$ K, then empirical evidence [4,5] suggests that submicron-sized MGs may sustain higher measurable σ_{peak} than BMGs of the same chemical composition, and thus $\sigma_{ideal} > \sigma_{peak}^{BMG}$. This, if true, would agree with the "smaller is stronger" trend in crystals, where σ_{ideal} can be approached, but never overtaken, by reducing the size of the sample or the size of the stressed region as in spherical nanoindentation of a half-space [2]. This possible "size dependence" of MG strength is the second conceptual question that this paper aims to address. As it turns out, the question of "size dependence" is deeply entangled with the question of initial condition sensitivity (this is also true for crystals [6]). Depending on the statistical specification of the IC of MG samples, one may or may not obtain size-dependent strength. This will be borne out by our simulations. In particular, we will explore different initial defect/flaw/damage populations in a MG sample, including, but not limited to, surface softening/hardening layers due to chemical implantation (e.g. from focused ion beam (FIB)), surface notches, pores and pre-existing internal shear bands [7]. These heterogeneous features (defects/flaws/damage) are called extended defects (a more formal definition will be given later), as they are above and beyond the intrinsic heterogeneities of the glass structure, and must be created extrinsically during thermomechanical processing, such as surface roughness due to casting, FIB and/or corrosion, shear bands due to unintentional impact in handling and/or previous mechanical service, or irradiation. In fact, contradicting conclusions [8] on the size dependence of the strength of MG nanosamples may imply that these laboratory-made samples could be far away from a "flawless" IC [9].

To address the above questions we will take a commonly accepted picture of how MGs deform, namely by shear transformation zones (STZs) that couple to each other by microelasticity [10,11]. The STZs are ~ 1 nm in size for common MGs based on atomistic simulations [12], and are the smallest units of inelastic deformation. They are inherently heterogeneous, with different shear options

(event menus) even before any macroscopic deformation is applied, reflecting the intrinsic heterogeneity and structural randomness (lack of long-range order) that define a glass [13]. In STZ dynamics simulation, unlike traditional continuum meshing approaches, the STZ size is fixed and not arbitrarily changeable like the finite-element meshes. For each individual STZ, one defines history-dependent local shear event menus that list random shear options even before thermal fluctuation is added, with effects such as damage accumulation, shear-softening (rejuvenation), damage repair (aging), dilation, heat generation, temperature diffusion and extreme-damage-induced cavitation. One then runs kinetic Monte Carlo (kMC) simulations on these spatially randomized STZs, where each STZ may be activated by the local stress and temperature, with the global stress and temperature fields satisfying continuum conservation laws. In STZ dynamics simulation, while one is mindful of atomistics, the atomistic details are coarse-grained and abstracted. We believe that such an STZ dynamics model provides sufficient basis to address the two conceptual questions posed above.

This paper is organized as follows. In Section 2.1 we introduce the numerical scheme of STZ dynamics simulation [13], now allowing elastic modulus inhomogeneity so that free surfaces, voids, etc., can be present in the simulations. In Section 2.2 different types of possible pre-existing defects/flaws/damages are described, and geometrical prescriptions and statistical models are established, which are closely related to the size dependence. In Section 3 the results of the simulations are described. In Section 4 we discuss the meaning of our results and address the two conceptual questions.

2. Theory and simulation methods

2.1. STZ dynamics model and inhomogeneous elasticity solver

The basics of our model are illustrated in Fig. 1. Each voxel (volume element) is considered as a potential STZ which could undergo certain inelastic transformation selected from a specific event catalog. Once a transformation occurs, we say that this voxel is undergoing a generation change $g \rightarrow g+1$, meaning that there is an internal structural change among atoms of this cluster, even after the "trivial" thermal vibrations and elastic displacements are filtered out [13]. Due to the disordered nature of glasses, voxels sit at different locations, e.g. A and B in Fig. 1 will have different event catalogs as indicated by the first two generation changes, i.e. $0 \rightarrow 1$ and $1 \rightarrow 2$ for both A and B. Each transition path, indicated by an arrow pointing to a potential transition state (dotted parallelogram) from the current generation, is described in our mesoscale model by a characteristic stress-free transformation strain (SFTS) tensor [14] $\boldsymbol{\epsilon}^{(m)}_{g\rightarrow g+1}$ and the corresponding activation energy barrier $Q^{(m)}_{g\rightarrow g+1}$. The "state-to-state" transition rate associated with this thermally activated STZ transformation is then given by $k^{(m)}_{g\rightarrow g+1} = \nu_0 \exp(-Q^{(m)}_{g\rightarrow g+1}/k_{\mathrm{B}}T), \quad m = 1,2,\ldots,\mathcal{M}$, where ν_0 is the attempt frequency of the order of the Debye frequency, k_{B} and T are the Boltzmann constant and temperature, respectively, and $\mathcal{M}$ is the total number of transformation modes one generation change can have. (This is essentially a topological parameter of the potential energy landscape and its determination would ultimately rely on atomistic simulations [13]. Here we use $\mathcal{M} = 60$ in our current 3-D simulations.) Then the kMC algorithm will evolve the system according to these defined transition rates and simulate the dynamics over a much longer time scale than atomic simulations. The key procedure in all kMC STZ models [10,11,15] is thus reduced to formulating the activation energy $Q^{(m)}$. In our model, this is given as:

$$Q^{(m)}_{g\rightarrow g+1} = \Delta F^* \exp(-\eta_g) - \frac{1}{2} V_g \boldsymbol{\sigma}_g : \epsilon^{(m)}_{g\rightarrow g+1}, \tag{1}$$

where ΔF^* is the Helmholtz free energy difference between the initial and the saddle-point configuration, and is modified by a scalar η_g which represents the amount of local softening at generation g and serves as a state variable to describe the local structure of the glass. (η_g essentially serves as local "free volume" in the voxel. See Section 4.6 for free-volume connectivity analysis using $\{\eta_g\}$ of voxels.) V_g is the atomic volume at the generation-g configuration. $\boldsymbol{\sigma}_g$ represents the local stress due to the heterogeneous plastic strain distribution and will bias the subsequent STZ transformations. Reciprocally, the transformations will alter the local stress by the Eshelby formalism [14], and it is through such dynamic interactions that the system reaches a macroscopic deformation pattern, e.g. shear localization or homogeneous deformation.

The configuration at generation-g $\mathbf{S}_g$ is then completely defined by [13]:

$$\mathbf{S}_g(\mathbf{x}) \leftarrow \left\{ \{\boldsymbol{\epsilon}^{(m)}_{g\rightarrow g+1}\}^{\mathcal{M}}_{m=1}, \boldsymbol{\epsilon}_g(\mathbf{x}), \boldsymbol{\sigma}_g(\mathbf{x}), \eta_g(\mathbf{x}), t^{\mathrm{elap}}_g(\mathbf{x}) \right\}, \tag{2}$$

where $\mathbf{x}$ represents the spatial position and $\boldsymbol{\varepsilon}$ is the accumulated inelastic transformation strain field. t^{elap} is another structural order parameter indicating how much time has elapsed since the last STZ transformation at $\mathbf{x}$. The subscript g indicates the current generation count. Defining IC for a MG sample in our model then involves prescribing $\mathbf{S}_{g=0}$.

The simplest $\mathbf{S}_{g=0}$ may correspond to setting the inelastic transformation strain field $\boldsymbol{\varepsilon}_{g=0}$ and the local stress field $\boldsymbol{\sigma}_{g=0}$ to zero, and the softening parameter $\eta_{g=0}$ to zero with a well-annealed history, i.e. $t^{\mathrm{elap}}_{g=0} \gg \tau$, where τ represents a characteristic relaxation such as β relaxation [16]. However, because the prior $\{\boldsymbol{\epsilon}^{(m)}_{0\rightarrow 1}\}^{\mathcal{M}}_{m=1}$ is heterogeneously randomized, there is still an inherent randomness built into our model.

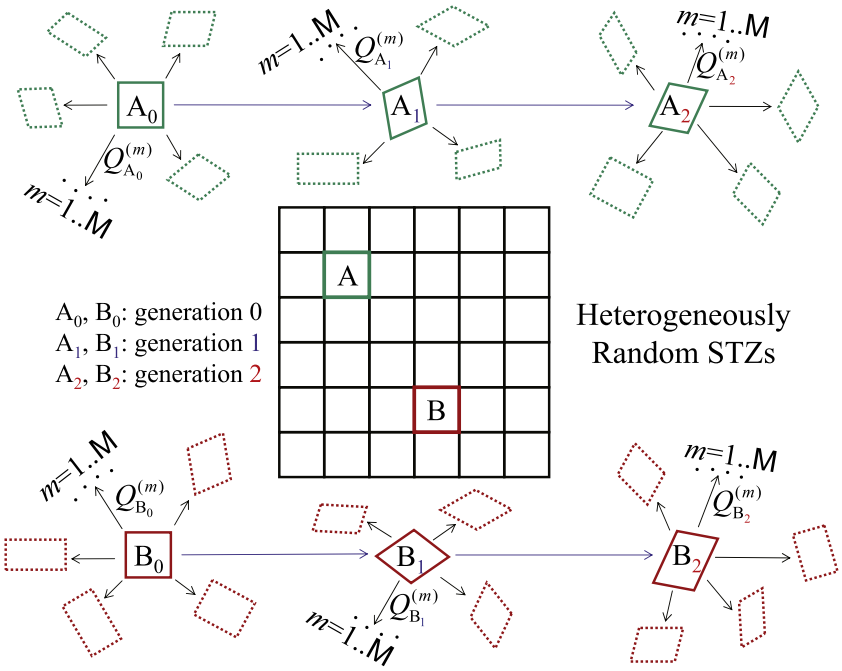

Fig. 1. Illustration of the heterogeneously randomized STZ model (cf. Fig. 1b of Ref. [10]). $Q^{(m)}$ is the activation free energy for a voxel to transform in the mth mode.

In 3-D simulations, we need to assign 3×3 matrices with the trace being zero to SFTS $\boldsymbol{\epsilon}^{(m)}_{g \to g+1}$. The SFTS is the model input which is drawn from certain numerical distributions confirmed by MD simulations [17]. The inherent structural isotropy of glass is preserved by drawing SFTS in a way such that the distribution of any strain component is invariant under arbitrary rotations. A detailed discussion and proof of the isotropic distribution is presented in Appendix A. We also want to study finite-sized samples by applying our previous transformation elasticity solver to an elastically inhomogeneous system. This is done following the approach of phase-field microelasticity theory [18] where a one-to-one mapping between a given inhomogeneous system and a virtual homogeneous system is uniquely established. Based on a recursive algorithm in Fourier space, we can solve the elastically inhomogeneous problem by essentially solving a homogeneous one. However, there could be an efficiency issue and we can use a Fourier-space filter to achieve faster convergence. A detailed derivation and a test of our solver are presented in Appendix B.

2.2. Pre-existing damage and extended defects

The main difficulty that prevents us from establishing a quantitative theory for MGs as a counterpart of dislocation theory in crystalline materials is the lack of experimental and theoretical characterizations of "microstructures", or mesoscale defects/flaws/damages, in MGs (what we called ICs in the Introduction). These microstructures are hereinafter called extended defects, which are heterogeneous features above and beyond what may be considered as the intrinsic heterogeneities of the glass structure. As "extended defect" is the central conceptual construct of this paper and is closely tied to the definition of ideal strength, which pertains to the so-called "reference glass" configuration, a more careful definition based on atomistic geometry is given below.

Let us first consider a definition scheme of extended defects in crystalline materials, using an atomistic construct of "free volume". We will not delve into the details of how an atomistic "free volume" may be defined, e.g. by constructing a Voronoi polyhedron around each atom. We are simply going to assume that we can define such a scalar for each atom. Since a defect in crystal may be 0-D (point defect), 1-D (dislocation), 2-D (grain boundary, crack) or 3-D (void), the connectivities between the atomistic free volumes are important. We may thus define the "connected atomistic free volume" (CAFV) to characterize the extent of percolation of free volume. Again, let us not delve into the details of how this may be done, given the atomic positions $\mathbf{x}^{3N}$. Methods already exist to label vacancies, interstitials, dislocation cores, etc., in crystalline metals if the atomic positions are given [19].

Free volume can be either positive or negative. Near vacancies (lower atomic coordination number than usual), free volume is positive. Near interstitials (higher atomic coordination than usual), free volume is negative. Atoms in a perfect crystalline region, by definition, should have zero free volume. Experimentally, free volume may be measured by positron annihilation spectroscopy [20]. Free volume distribution could also give rise to a degree of image contrast in transmission electron microscopy [21,22],

enabling shear bands in MGs to be experimentally identified [23].

Now imagine that we take a crystalline metal—not a perfect crystal but a "realistic" crystalline metal—and cool it down to 0 K. We obtain the so-called inherent structure [24] configuration, where thermal vibrations are excluded. If one performs CAFV analysis on this configuration, and count the occurrence of atoms by their closest CAFV, one expects a distribution like that shown in Fig. 2. Most of the atoms have zero CAFV nearby, and thus are represented by the delta-function peak at 0 $Å^3$. Some atoms are adjacent to vacancies, and some atoms are adjacent to interstitials, so there can be some counts at, say, $\sim \pm 12$ $Å^3$, which is one atomic volume. Note that the equilibrium concentration of vacancies or interstitials at 0 K is zero, but real metals tend to be out-of-equilibrium, with quenched-in vacancies and/or interstitials. Atoms in dislocation cores and grain boundaries are adjacent to even larger percolating free volume, and are labeled by the other peaks in Fig. 2. The reason why ideal strength is easy to define for crystalline materials is that there is a distinct gap between the 0 $Å^3$ sharp peak and the nearest $\pm 12 Å^3$ sharp peaks, and there is no other CAFV possibility in between. In other words, it is very obvious where the point defects and extended defects are in a crystal. There is no continuum of metastable atomic geometries between 0 $Å^3$ and ± 12 $Å^3$, which then allow us to unambiguously define a "reference" configuration: the perfect crystal. The ideal strength is defined based on when this theoretical reference crystal can be made unstable at 0 K.

The difficulty with defining the ideal strength of glass stems from the uncertainty of how to define a "reference glass" configuration, or glass configurations with only "intrinsic" but no "extrinsic" heterogeneities. To clarify the issue at hand, we illustrate the CAFV spectrum of a real MG in Fig. 2. We know that glass by definition has an out-of-equilibrium structure and lacks long-range order. Therefore atomic structural fluctuations reflected by either positive or negative CAFV exist intrinsically, which also has a smooth distribution instead of a sharp delta-function-like peak [25]. However, we expect the range of this "natural" or intrinsic CAFV distribution during a well-controlled cooling process from liquid melt to be limited to the level of the atomic volume ($\pm \sim 12$ $Å^3$). Extended defects, on the other hand, characterize something significantly bigger than mere atomic-volume-scale CAFV and are much more collective structural alterations. Without external mechanical–chemical driving forces much more potent than $k_B T$ strongly driving the system (e.g. surface roughness due to casting, FIB, corrosion, shear bands due to previous mechanical service, high-energy irradiation), such large CAFV should never exist in the configuration. This origin of "extrinsic" heterogeneities in MGs is similar to dislocations which are essentially mechanically driven, out-of-thermal-equilibrium defects (the thermal equilibrium population of extended dislocation lines in crystals should be zero at zero stress due to infinite formation energy). Also, because of such a large percolating free volume, atoms near the extended defects possess significantly softer vibrational "modulus" and may be under significant residual stress as well as an external stress amplification factor. Atoms near extended defects are therefore much easier to dislodge by applying an external stress to the entire system. The above descriptions, though still not as quantitative as we would like, provide a more concrete definition of "extrinsic" heterogeneities of glasses, hereinafter called extended defects in glasses.

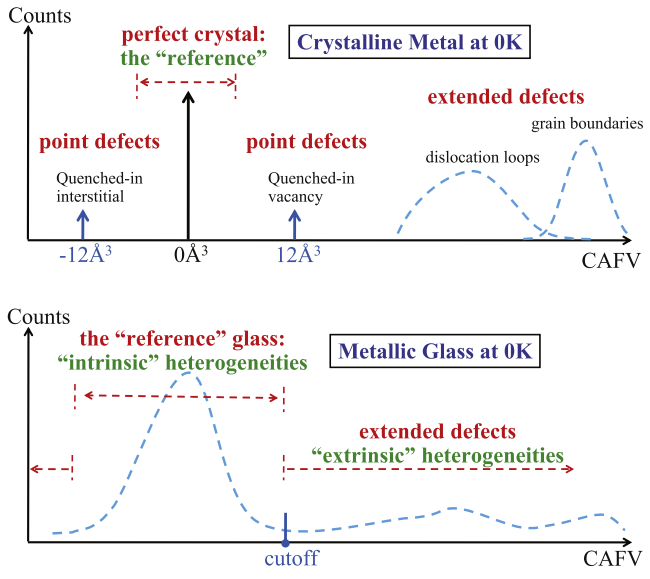

Fig. 2. Schematic results of "connected atomistic free volume" (CAFV) analysis on crystalline metals and MGs at 0 K.

If there is a true gap in the CAFV spectrum that allows a clean separation between the intrinsic heterogeneities and the extended defects, then our job is easier. In the worst case of no absolute gap, such as that illustrated in Fig. 2, we nonetheless can pick a reasonable cutoff in CAFV, e.g. tens of atomic volume, to separate what is considered intrinsic from extrinsic heterogeneities. The cutoff should be chosen such that with a well-administered cooling schedule from liquid melt, under the PBC in all three directions without free surfaces, a CAFV of this magnitude cannot be produced even in a macroscopic volume of MG. (In other words, to create CAFV above this magnitude, some other mechanical-chemical driving force or thermal gradient must be applied.) With the CAFV cutoff thus chosen, we then have a definition of atomic regions containing extended defects, and atomic regions without any extended defect. Thus a definition of "reference glass" is provided, which is a macroscopic volume of glass without any extended defect, including surfaces. This is a reference material that is very difficult to obtain in reality. But so is the perfect crystal on which Frenkel developed his concept of ideal shear strength. Ideal strength, or theoretical strength, is just a theoretical construct, the result of a thought experiment, that can have bearing on real experiments in the limiting sense [2]. Let $\mathbf{x}_{\mathrm{ref}}^{3N}$, where N is the total

number of atoms, denote the "reference glass" configuration above. $\mathbf{x}^{3N}_{\text{ref}}$ is a $T = 0$ K inherent structure [24], a metastable point on the potential energy landscape $U(\mathbf{x}^{3N})$. We should also consider the large-size limit in all three directions for the PBC supercell, $N \to \infty$. Consequently, the intensive properties that pertain to $\mathbf{x}^{3N}_{\text{ref}}$ should have no T or N dependence. However, $\mathbf{x}^{3N}_{\text{ref}}$ is produced by a hypothetical MD procedure under PBC (liquid cooling to 0 K in a large PBC supercell) that depends on the cooling rate $-\dot{T}$. Hence, $\mathbf{x}^{3N}_{\text{ref}}$ is a function of the cooling rate used to produce it:

$$\mathbf{x}^{3N}_{\text{ref}} = \mathbf{x}^{3N}_{\text{ref}}(-\dot{T}). \tag{3}$$

This macroscopic "perfect glass" or "reference glass" $\mathbf{x}^{3N}_{\text{ref}}$ without any extended defect, where atomic-level structural variations and residual stresses [13,25] exist but are not yet collective or extended, then allows us to define the ideal strength σ_{ideal} of the glass. Imagine a thought experiment where stress σ on a macroscopic "reference glass" $\mathbf{x}^{3N}_{\text{ref}}$ is ramped up from zero, and the temperature is maintained at 0 K such that no thermal activation is possible. At some point there will be a bifurcation instability, where a particular lattice vibrational eigenmode turns imaginary. However, unlike in perfect crystals, where the first lattice instability most often leads to large-scale stress relaxation by dislocation loop or crack nucleation followed by ballistic motion along crystallographic directions [26], in MGs such instabilities are often arrested in a local region due to rapid decay of residual stress, and may not have much consequence at the macroscopic stress–strain level. Thus, using the very first vibrational instability to define σ_{ideal} may not lead to a very useful concept. A better definition of σ_{ideal} could be to allow the first, second, third, etc., local instabilities to develop and arrest if they can be arrested in MD, as σ on the macroscopic "reference glass" $\mathbf{x}^{3N}_{\text{ref}}$ is ramped from 0 to σ_{ideal} quasi-statically, at $T = 0$ K. With each local instability that arrests, the MG lands in a different inherent structure [24], and then the stress continues to ramp up (while maintained at 0 K) until at σ_{ideal} the local instabilities percolate and go global. Thus, σ_{ideal} is defined by the point of the first global instability, with stress ramping from zero on the macroscopic "reference glass". What we expect to happen at 0 K is that at σ_{ideal}, an extended defect (flow defect) nucleates out of the "perfect glass" or "reference glass" and finally breaks into the macroscale. In other words, σ_{ideal} is defined by CAFV $\to \infty$ from a starting sample that initially does not have any larger-than-intrinsic CAFV (the "reference glass" initial condition) with a quasi-static stress-ramp at 0 K. We call such a definition scheme of the ideal strength of glass the "percolation threshold" definition for σ_{ideal}. From now on we will use the term "perfect glass", "reference glass" or $\mathbf{x}^{3N}_{\text{ref}}$ interchangeably. σ_{ideal} pertains to $\mathbf{x}^{3N}_{\text{ref}}$, and since $\mathbf{x}^{3N}_{\text{ref}}$ depends on the cooling rate used to produce it, σ_{ideal} is also a function of the cooling rate:

$$\sigma_{\text{ideal}} = \sigma_{\text{ideal}}\left(\mathbf{x}^{3N}_{\text{ref}}(-\dot{T})\right) = \sigma_{\text{ideal}}(-\dot{T}). \tag{4}$$

If pre-existing defects/damage/flaws exist in a MG, the CAFV spectrum extends beyond the cutoff labeled in Fig. 2. Unlike crystalline metals, where different types of extended defects, e.g. dislocations and grain boundaries, have been meticulously studied experimentally, the extended defects in MGs are less well characterized experimentally. They are illustrated on the CAFV spectrum by the broad peaks, which should depend on processing and service history. For instance, larger pores should correspond to a peak with larger characteristic CAFV. In Fig. 3(a) two types of extended defects, A and B (with different characteristic CAFVs illustrated as the differently shaded defect volumes), are assumed in a MG. An average defect spacing, i.e. L_{A} and L_{B}, is also defined in Fig. 3(a), which is inversely proportional to the density of the corresponding defect, i.e. $\rho_{\text{A}} \equiv L_{\text{A}}^{-3}$ and $\rho_{\text{B}} \equiv L_{\text{B}}^{-3}$.

We will address the effect of size on the actual strength and connected-free-volume spectral evolution using kMC simulations in the remainder of the paper. Before doing the simulations, however, we build a toy model to illustrate the size dependence. Since mechanical behaviors such as yielding and failure depend on the extended defect population, which fluctuates considerably, especially in submicron samples where the total number of these extended defects is small, a statistical approach such as that used in Ref. [27] is needed. For illustration, let us assume a finite-sized MG with volume V, which could be on the submicron scale, will be tested under just two sequential stresses, σ_{bulk} and σ_{ideal}, where σ_{bulk} is the bulk strength (measured for $V \to \infty$ with the same CAFV spectrum). If the finite-V sample survives the first σ_{bulk} test, it certainly will not survive the second σ_{ideal} test. We look at the failure/yielding statistics of an ensemble of finite-V samples, and define the ensemble-average strength to be:

$$\sigma_{\text{avg}}(V) = \sigma_{\text{ideal}}P(V) + \sigma_{\text{bulk}}(1 - P(V)), \tag{5}$$

where $P(V)$ is the probability that a finite-V sample survives the first σ_{bulk}-test.

Consider the following hypothesis: a single defect A means "fatality" at σ_{bulk}. In other words, under externally applied σ_{bulk}, a single defect A appearing anywhere in the sample would cause the entire sample to fail. The survival probability due to possible presence of A is then (based on Poisson statistics):

$$P_{\text{A}} = \exp(-\rho_{\text{A}}V). \tag{6}$$

Clearly, as long as $\rho_{\text{A}} > 0$, the bulk sample ($V \to \infty$) always fails at σ_{bulk} because it will always contain at least one A. We can define the concept of critical count, N^{c}_{A}, which is the total count of a certain defect in the entire sample volume to cause global failure. The physical basis for $N^{\text{c}}_{\text{A}} = 1$ (independent of volume) is that a single defect of sufficiently large CAFV could cause an entire sample to fail. For instance, A could be a sufficiently long crack to exceed the fracture toughness of this MG at σ_{bulk}.

Not all damages act like A, however. If A symbolizes the penultimate "crack"-like behavior, there is also a

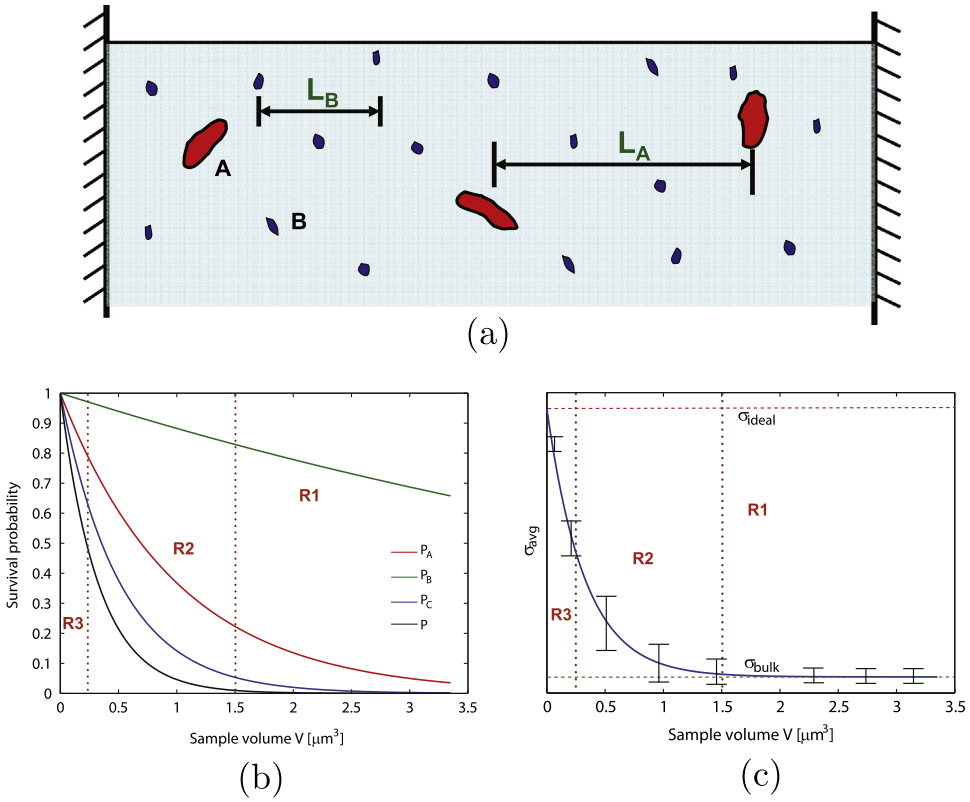

Fig. 3. (a) Illustration of two types of extended defect, A and B, with the corresponding characteristic defect spacing L_A and L_B, respectively. Three extended defects characterizing different failure behaviors are considered, and (b) the survival probability and (c) ensemble-averaged strength are obtained based on our statistical model.

penultimate "ductile" failure behavior, to be symbolized by B, with $N_B^c \propto V$. In other words, global failure would not occur unless the volumetric density (not the total number) of B-type damage exceeds a critical threshold. In this case, the critical count for B would be:

$$N_B^c = \lceil \rho_B^c V \rceil, \tag{7}$$

where $\lceil \cdot \rceil$ rounds a real number to the nearest integer above. The physical meaning of B is that damages such as a small STZ or void cannot fail the entire material on its own; they need to reach a critical damage density at σ_{bulk} to cause global failure.

We can also model the intermediate behavior between penultimate "crack" and penultimate "ductile" failure, by fitting the critical count to a power-law:

$$N_C^c = \left\lceil \left(\frac{V}{V_C} \right)^{\alpha_C} \right\rceil, \tag{8}$$

where V_C and α_C are two parameters characterizing the fatality of defect C population. As intermediate between the two extreme behaviors of A ($\alpha_A = 0$) and B ($\alpha_B = 1$), we should have the exponent $0 \leqslant \alpha_C \leqslant 1$. Based on this general fitting form, the survival probability due to C is:

$$P_C = \sum_{i=0}^{N_C^c - 1} \frac{\exp(-\rho_c V)(\rho_c V)^i}{i!} = 1 - \sum_{i=N_C^c}^{\infty} \frac{\exp(-\rho_c V)(\rho_c V)^i}{i!}. \tag{9}$$

according to Poisson statistics.

Assuming that different defect populations do not interact (in reality they do), the total survival probability can be written as:

$$P(V) = \prod_s P_s(V), \tag{10}$$

where $s = A, B, C, \ldots$, labels the extended defect type, and

$$P_s(V) = \sum_{i=0}^{\left\lceil \left(\frac{V}{V_s}\right)^{\alpha_s} \right\rceil - 1} \frac{\exp(-\rho_s V)(\rho_s V)^i}{i!}. \tag{11}$$

In Fig. 3(b), if we assume $N_A^c = 1$ ($\alpha_A = 0$), $L_A = 1$ μm; $L_B = 2$ μm, $\rho_B^c = 1.2\rho_B$ ($\alpha_B = 1$); $\alpha_C = 0.5, L_C = 0.8$ μm, $V_C = 10L_C^3$, the ensemble-averaged strength $\sigma_{avg}(V)$ given by Eq. (5) is plotted as a function of $V \equiv L^3$.

Three regimes may be divided based on the probability shown in Fig. 3(b). In R1 the sample size is large enough such that it can always have sufficient extended defects to facilitate failure/yielding, e.g. shear bands may be heterogeneously nucleated from pre-existing defects with a moderate amount of applied stress. In R2 the probability of having defects decreases "significantly" as the sample size shrinks. This implies that the nucleation of shear bands is not as easy as in R1. Thus we might expect "smaller is stronger" with more stochastic scattering on the measurement. When sample sizes reduce down to the region of R3, the probability of having sufficient initial extended defects that facilitate yielding becomes very low. The

majority of samples in R3 are "damage free" and the yield strength is bounded by that required for nucleation of shear bands in the "reference glass". Based on Eq. (5), we can preliminarily propose a size-dependent strength as shown in Fig. 3(c), where error bars indicate scatter of the measured strength with certain (e.g. 90%) confidence intervals.

The above division may not be quantitative. However, the main basis for such dividing is the survival probability of the possible extended defects. The R1 and R3 simply correspond to the two extreme cases with the probability approaching 1 and 0, respectively. Experiments performed within these two regions will show a specific strength with relatively little scatter, while in between the data will exhibit large scatter. This is especially the case for crystals, where σ_{bulk} and σ_{ideal} are hugely different. For MGs, in principle, this should also be the case, but may not be that obvious as in crystals, since σ_{bulk} and σ_{ideal} are only $\sim 3\times$ different at most.

2.3. Sample preparation and initial conditions

Each voxel in our 3-D Cartesian computational grid has a physical size of 1.5 nm × 1.5 nm × 1.5 nm, a characteristic size of a STZ [3,28,29]. We can either apply PBC in all three directions to obtain the bulk samples, or designate several outermost layers of y- and z-dimensions as "air" (by assigning zero elastic modulus) to generate finite-sized samples that exhibit a "nanobar" geometry with the x-axis being the longitudinal direction along which uniaxial tension will be applied.

The simplest IC we can consider has local inelastic strain, stress and softening fields zero everywhere: $\boldsymbol{\varepsilon}_{g=0} = 0$, $\boldsymbol{\sigma}_{g=0} = 0, \eta_{g=0} = 0$ and $t^{\text{elap}}_{g=0} \gg \tau$ in Eq. (2). We label this state as $\mathbf{IC}_1$. Note that $\mathbf{IC}_1$ does not correspond to the aforementioned "reference glass" configuration $\mathbf{x}^{3N}_{\text{ref}}(-\dot{T})$, since $\mathbf{x}^{3N}_{\text{ref}}$ likely involves significant residual stress fluctuations [25] even for experimental cooling rate of producing glasses. But $\mathbf{IC}_1$ is something simple enough that we can start with. See the end of Section 5 for discussions about this issue.

The introduction of extended defects requires careful consideration, since we have no direct experimental information about the exact damages/flaws in realistic MGs corresponding to the CAFV spectrum beyond the cutoff, as experimental characterization of extended defects is far less developed as compared to that in crystals. For simulations, even though it is reasonable to expect groups of activated STZs as a candidate, we still need to consider how they should be populated spatially. Apart from this, the internal stress field should satisfy the self-equilibrium condition such that the initial sample is macroscopically stress-free. Analogous to what some modelers do for crystals when they do not want to deal with placing atoms according to anisotropic elasticity theory of dislocations explicitly, we apply a certain amount of pre-strain ($\sim 3\%$ elongation along the x-axis at a strain rate $10^{-4}\ \text{s}^{-1}$) to $\mathbf{IC}_1$ finite-sized samples and then remove the external load. If the pre-strain is sufficient to induce plastic deformation, we would expect some STZs have been locally activated, or even percolated through to form a connected cluster, resulting in an internal residual stress field that may promote STZ transformations subsequently at finite temperature. We then use the kMC method to "anneal" this pre-strained sample at room temperature to ensure that thermally activated STZs at zero external stress would require a sufficiently long waiting time as compared to the duration of our following tensile test simulations (up to 6% total elongation with a strain rate $10^{-4}\ \text{s}^{-1}$). Samples prepared according to such a "pre-straining and relaxation" scheme are labeled as $\mathbf{IC}_2$.

Free surface is also an important class of extended defects [30]. MD simulations have found lower potential energy barriers for STZs at surfaces [31], suggesting an inherent difference in transformation energetics compared to the bulk. In addition, techniques used to prepare nanoscale samples may also introduce chemical and structural heterogeneities that are mainly localized near surfaces. For instance, FIB milling can alter the defect content and defect chemistry of crystalline samples by introducing dislocations, implanted ions and amorphization [32], resulting in local hardening [33] in a layer adjacent to the milled surface, but it could be softening as well depending on the details of the ion beam milling. Recently, the influence of gallium contamination from FIB milling on shear band formation in nanoscale MGs has also been considered experimentally [9,34]. To simulate the surface contamination, we assume that the activation barriers for STZs near surfaces could be different from that in the bulk. In particular, as a parametric study, we consider two opposite cases where the stress-free activation barrier ΔF^* is either 3 or 7 eV (the bulk value is 5 eV) for the outermost STZ layer, the so-called "surface softening" ($\mathbf{IC}_3$) or "surface hardening" ($\mathbf{IC}_4$) IC, respectively.

The material properties used in the following simulations are listed in Table 2. The Young's modulus and Poisson ratio are taken from amorphous alloy $Zr_{52.5}Cu_{17.9}Ni_{14.6}Al_{10}Ti_5$ [35]. Detailed physical meanings of the simulation parameters listed in Table 2 can be found in Ref. [13].

3. Results

We first present the result of $\mathbf{IC}_1$ bulk, serving as a comparison with cases of finite-sized samples. Fig. 4(d) shows the stress–strain curve obtained in the simulated tensile test

Table 1
Different initial conditions used in simulations.

Simulation initial condition	Meaning/method
$\mathbf{IC}_1$	The simplest glass
$\mathbf{IC}_2$	Pre-strain and relaxation
$\mathbf{IC}_3$	Surface STZ "softening"
$\mathbf{IC}_4$	Surface STZ "hardening"

Table 2
List of simulation parameters [13].

Parameter	Value	Meaning
E	88.6 GPa [35]	Young's modulus
ν	0.371 [35]	Poisson ratio
ν_0	1×10^{13} Hz	Trial frequency of STZ
ΔF^*	5 eV	Stress-free activation energy barrier of STZ
Q_{act}	0.37 eV [36]	Activation energy barrier for local relaxation
κ_p	10	Permanent softening coefficient
κ_t	30	Temporary softening coefficient
γ^*	0.1 [37,38]	Characteristic shear transformation strain of STZ
T	300 K	Temperature
$\dot{\bar{\varepsilon}}$	1×10^{-4} s^{-1}	Applied strain rate
$d\bar{\varepsilon}$	1×10^{-4}	Strain increment of each simulation step

with a computational supercell of 192 nm × 96 nm × 96 nm. Fig. 4(a) and (b) plots, in surface and contour representations, respectively, the distribution of von Mises strain after 10% elongation, showing a dominant shear band being formed in one of the maximum shear stress planes. We point out that our model, for simplicity, prescribes a finite softening without local heating or cavitation, and therefore does not consider an ultimate failure scenario [39,40]. This leads to indefinite continuation of the stress–strain curve, as shown in Fig. 4(d). If we do allow the local softening to go to infinity by heating beyond the glass transition temperature T_g and/or cavitation, the shear band will "run wild" after the stress drop at the peak stress σ_{peak}, and eventually develop into a genuine shear crack [39,40].

To investigate the effects of sample size and IC, we perform tensile test simulations on samples with different sizes and ICs. The obtained stress–strain curves are shown in Fig. 5. It is obvious that the peak stress σ_{peak} shows different size dependence in samples with different ICs. Here we employ the term "peak stress" instead of "yield strength" because for small-volume MGs it is difficult to define the yield point unambiguously and the peak stress σ_{peak} is one of the principal parameters that characterize the strength of MGs [41]. For $\mathbf{IC}_1$ samples, σ_{peak} is independent of sample size, and is actually the same as that of the $\mathbf{IC}_1$ bulk (Fig. 5(a)). However, $\mathbf{IC}_2$ samples exhibit a "smaller is stronger" trend, and the peak stresses of all these "realistic" samples are below that of the $\mathbf{IC}_1$ bulk. In addition, samples of $\mathbf{IC}_3$ and $\mathbf{IC}_4$ exhibit a "smaller is weaker" or "smaller is stronger" trend, respectively. These results show that the strength of a MG sample is determined by its initial condition as well as its size. If we extract the peak stress of the "more realistic" $\mathbf{IC}_2$ samples and plot them against the size, the result (Fig. 6) exhibits a size dependence that is similar to our preliminary proposal in

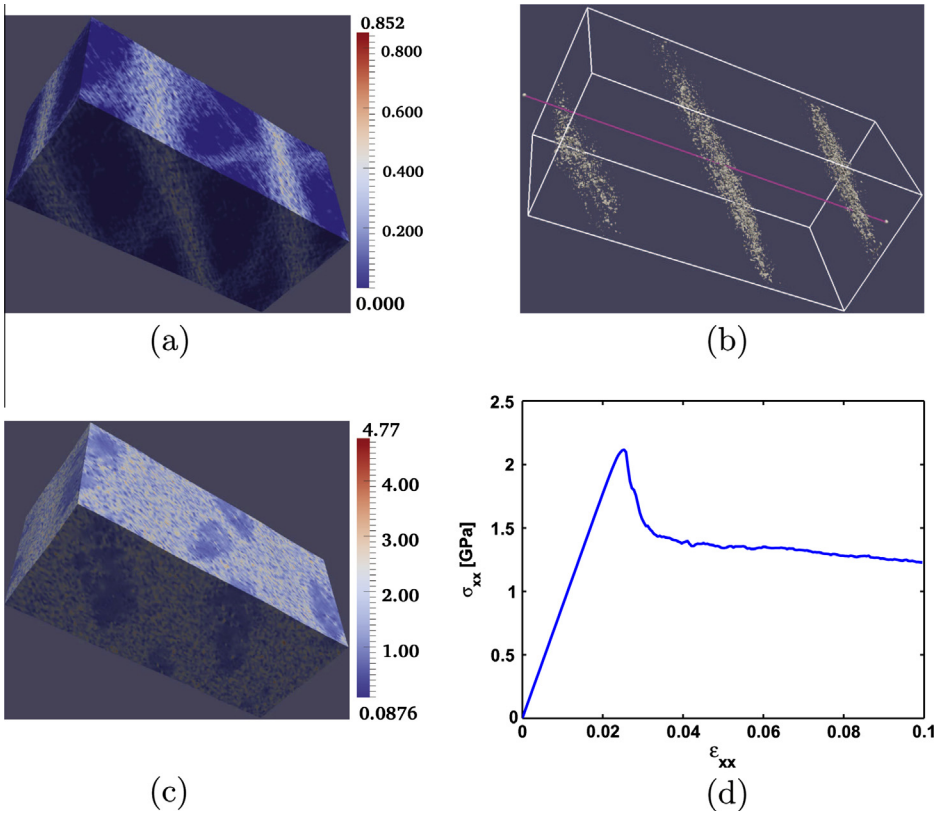

Fig. 4. Tensile test simulation on a $\mathbf{IC}_1$ bulk sample: von Mises strain distribution in (a) surface representation and (b) contour representation and (c) von Mises stress distribution in contour representation after 10% elongation; (d) the stress–strain curve.

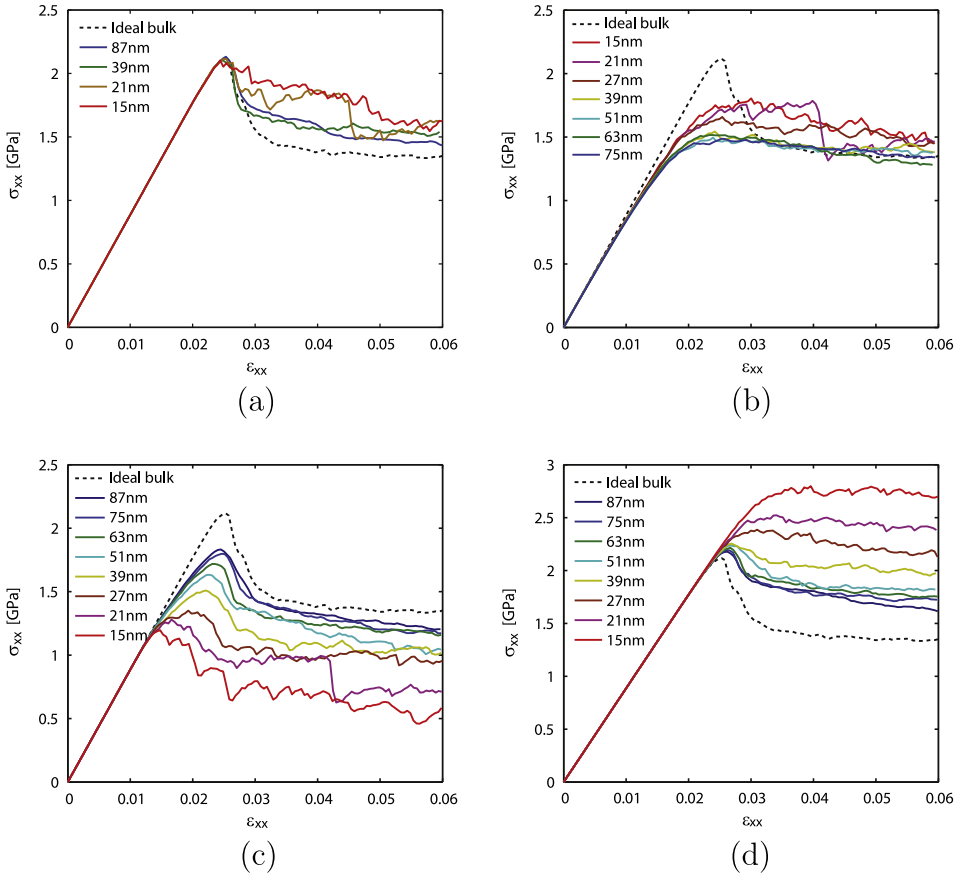

Fig. 5. Stress–strain curves for finite-sized samples with initial condition (a) $\mathbf{IC}_1$ ("ideal"), (b) $\mathbf{IC}_2$ (with pre-existing extended defects), (c) $\mathbf{IC}_3$ (with "surface softening") and (d) $\mathbf{IC}_4$ (with "surface hardening").

Fig. 3(c). To fully understand such a "smaller is stronger" phenomenon, the correlation between ICs and sample sizes needs to be clarified. This will be done in Section 4.

On the other hand, the flow stress σ_{flow}, defined as the stress required to sustain deformation after the peak stress has been reached, depends on the sample size for all ICs. In experiments (at room temperature), the time it takes from the peak stress to catastrophic failure is so short that the flow stress is difficult to measure. However, if the local stress could be measured and plotted against the local strain inside a shear band, there could be a significant stress–strain plateau (i.e. the flow stress) that is similar to our simulation results. Indeed, because of the inhomogeneous deformation, it is suggested that strain within the shear band could go to a much larger value (e.g. $\sim 1000\%$) than the overall strain [38].

Despite the serrated features shown in Fig. 5, the ranking of σ_{flow} can still be identified. For $\mathbf{IC}_1$ and $\mathbf{IC}_2$, smaller samples generally require higher σ_{flow}, while for $\mathbf{IC}_3$ and $\mathbf{IC}_4$, the trend is controlled by the nature of surface STZs. Since the properties of $\mathbf{IC}_3$ and $\mathbf{IC}_4$ samples are expected to be largely determined by the fraction of "contaminated" surface layers, we will analyze them separately in Section 4.

In order to understand the "smaller is stronger" trend in the simulated flow stress of $\mathbf{IC}_1$ and $\mathbf{IC}_2$ samples (Fig. 5(a) and (b)), we need to analyze the collective deformation mechanism underlying the flow. In Fig. 7 we plot the von Mises strain distribution at the applied strain of 3% (left column), 4% (middle column) and 6% (right column), for $\mathbf{IC}_1$ samples of 87 nm (top row), 21 nm (middle row) and 15 nm (bottom row), respectively. It is clear that the abrupt stress-drop for the 87 nm sample at $\sim 2.5\%$ applied strain

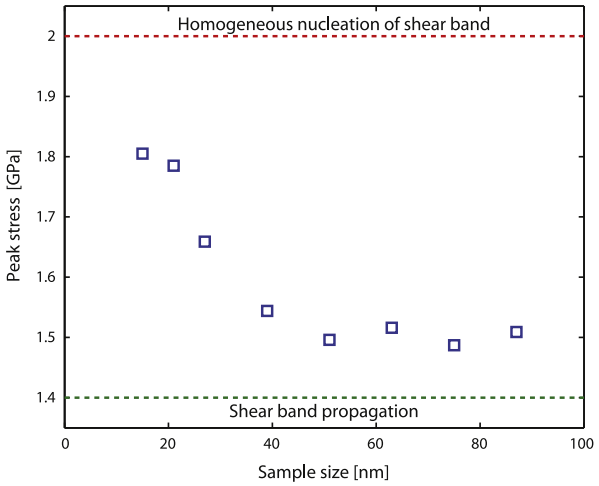

Fig. 6. Peak stress vs. sample size for $\mathbf{IC}_2$ finite-sized samples.

in Fig. 5(a) is associated with the nucleation of a shear band, as shown in Fig. 7(a). Because of strain-induced softening, deformation afterwards is carried out by STZ activation localized within and ahead of this nucleated shear band. Subsequently, the shear band grows along its own plane, which is one of the maximum shear stress planes under the applied tension. However, the surfaces place a geometric limit which prevents the runaway growth of shear band as in the bulk. This can be seen by comparing Fig. 7(a) with (b). In addition, we see that a secondary shear band, which intersects with the first one, is also formed in another maximum shear stress plane as the deformation continues, shown in Fig. 7(c).

The 21 nm sample also exhibits an abrupt stress-drop at the peak stress, as in the case of the 87 nm sample. However, the relatively smaller stress-drop suggests that the nucleated shear band could not reach the same level of "maturity" (i.e. runaway growth) as in the 87 nm sample, in the sense that the shear band is now confined to a much smaller spatial region and the corresponding CAFV is smaller than that of the shear band in larger samples. The resulting flow stress is thus maintained at a higher level as shown in Fig. 5(a). To accommodate further deformation, a secondary shear band needs to be formed, as in the case of the 87 nm sample. However, it is shown in Fig. 7(f) that the secondary shear band is spatially uncorrelated with the first one. This is attributed to the fact that the first "immature" shear band has not grown to a sufficient level (in terms of local softening and stress field) that could influence the nucleation of the secondary shear band in its vicinity, indicating a homogeneous nucleation scenario with a secondary abrupt stress-drop that is comparable to the initial one on the stress–strain curve in Fig. 5(a).

When the sample shrinks down to 15 nm, the spatial extent along the maximum shear stress plane is only $\sim$ 20 nm. Considering that shear bands usually have a characteristic thickness of $\sim$ 10–20 nm [42], the nucleated shear band will possess an aspect ratio of $\sim$ 1. From our simulation, the initially activated STZs are indeed more "spherically" distributed in space instead of forming a large-aspect-ratio planar region, as shown in Fig. 7(g). Another distinct feature is that at 3% applied strain, there have already been two clusters of activated STZs formed. Due to limited sample size, they can only grow in width in a more diffusive manner as shown in Fig. 7(h) and (i). Because of this essentially "diffusive spread" of STZ operations rather than a collective shear-banding, the flow stress decreases gradually in a continuous fashion without abrupt stress relaxations, contrasting previous cases (Fig. 5(a)).

The ranking of σ_{flow} for $\mathbf{IC}_2$ samples are similar to those discussed above. In fact, comparing the stress–strain curves for $\mathbf{IC}_1$ and $\mathbf{IC}_2$ in Fig. 5(a) and (b), apart from a shift-down of the flow stresses due to the pre-existing extended defects of $\mathbf{IC}_2$, the stress–strain curves closely resemble

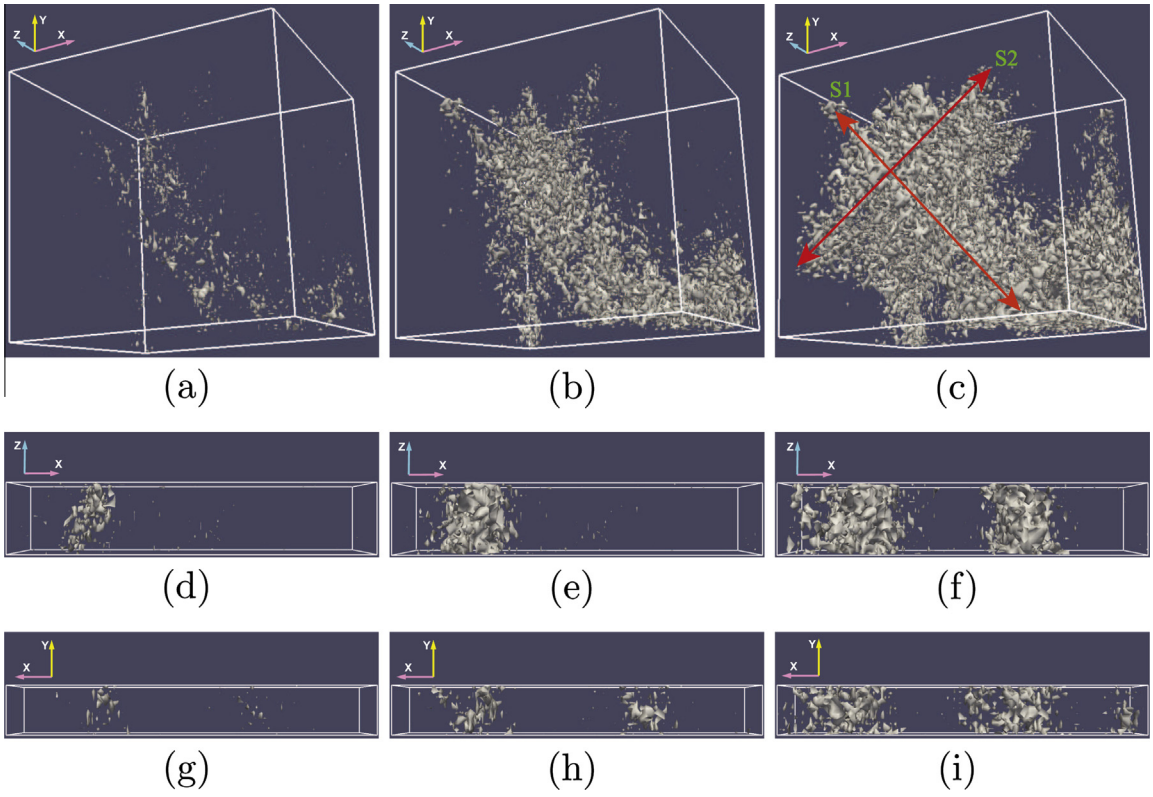

Fig. 7. Von Mises strain distributions plotted in contour representation at 3% (left column), 4% (middle column) and 6% (right column) elongation, for IC_1 samples with cross-sections of 87 nm × 87 nm (top row), 21 nm × 21 nm (middle row) and 15 nm × 15 nm (bottom row). The strain threshold is 0.14 for the first two rows and 0.12 for the last row.

each other for samples with the same size, implying similar deformation kinetics in the flowing regime.

4. Discussions

Our kMC simulation results contain rich information about MG deformation kinetics that needs to be mined and discussed. Below we will address shear band thickness, extreme value statistics [43], intersections of shear bands, and finally return to the connected-free-volume (CAFV/CFV) analysis that is the conceptual foundation of this paper.

4.1. Shear band thickening

The thickness of shear bands has been reported by previous experiments and simulations. In order to determine this fundamental structural feature, we plot the spatial variation of von Mises transformation strain along lines parallel to the tensile axis. (One such line is drawn in Fig. 4(b).) Fig. 8(a) shows such variations along lines intersecting with the shear band at different locations. All plots show that there is a region within which the von Mises strain is always larger than the average applied strain (10% in Fig. 8(a)). We may thus define the extent of such a region, wherein the von Mises strain of all voxels have exceeded the average applied strain, as the thickness of our simulated shear bands. Fig. 8(b) also shows the spatial variations at both 3% and 10% applied strain along the same line. The increase in von Mises strain in terms of both intensity and spatial extent indicates the growth of the shear band. Since experiments under uniaxial tension usually end around $\sim 3\%$ elongation due to the sudden failure of MG samples, we take the measurement at 3% applied strain as a characteristic thickness w for our simulated shear bands in the bulk. Measurements are carried out for supercells of different sizes and are reported in Table 3. It is seen that $w \approx 20$ nm, which agrees with most experimental measurements and atomistic modeling [42], and is also consistent with our previous 2-D simulations [13]. The fact that shear band thickening saturates at 20 nm and w does not increase much with further straining indicates significant softening inside due to free-volume-percolation, so much so that further deformation involves mostly atoms in the center and at the front, and not on the periphery side edges, of the existing shear band. A very rough estimate of the order of magnitude of the percolating-free-volume is:

$$\mathrm{CAFV} > (20\ \mathrm{nm})^3 \times 1\% \sim 100\ \mathrm{nm}^3, \tag{12}$$

where the $\sim 1\%$ dilation is estimated from atomistic simulation [39] and experiments [21]. This is about 10,000 atomic volumes, which can never be the natural or "intrinsic" kind of atomic structural heterogeneities.

4.2. Size-dependent deformation mode transition

Given a spatial constraint due to sample size or secondary phases that have a characteristic length scale l_0, it is expected that $l_0 \sim w$ should be a point for deformation mode transition, since shear bands with a high aspect ratio will never be able to develop under this geometric constraint, and plastic deformation is carried out by "diffusive spread" of STZ operations as shown in Fig. 7. Experiments [44,45] have suggested that a brittle-to-ductile transition could occur when samples shrink down to a critical size of $l_0 \sim 100$ nm, which is $5\times$ the shear band thickness $w \sim 20$ nm. This may be understood by the notion that a shear band with aspect ratio larger than 1 could still be stable even under moderate far-field stress, rather than acting like a runaway shear crack. In fact, MD simulations have revealed a critical aspect ratio of ~ 5 that an embryonic shear band could have before it becomes an unstable runaway [12]. This implies that as long as the maximum aspect ratio l_0/w does not exceed ~ 5, the sample could still sustain certain stable plastic deformation, and the ductility may be improved by proliferation of these short shear bands.

4.3. Extreme value statistics

In analyzing deformation of MGs at the STZ level, extreme value (EV) statistics [43] is expected to be crucial,

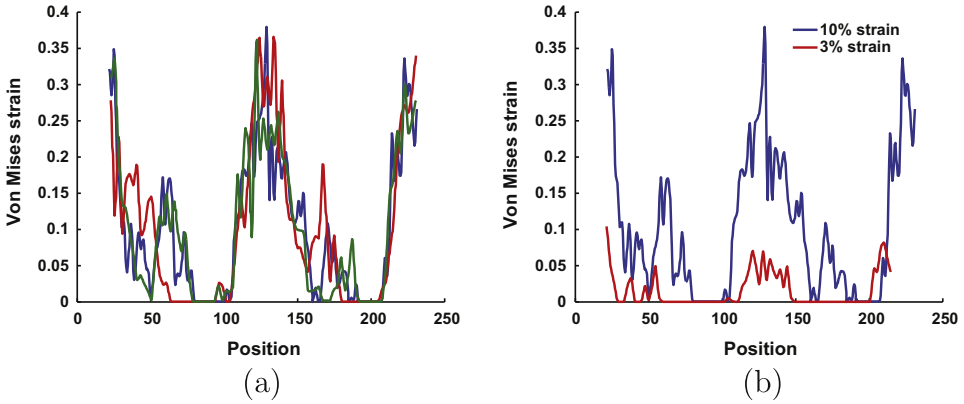

Fig. 8. Spatial variations of von Mises strain along the tensile axis: (a) at different locations when applied strain is 10%; and (b) at two different applied strains.

Table 3
The thickness of simulated shear band.

Supercell size (nm)	96 × 48 × 48	96 × 96 × 96	192 × 96 × 96
Thickness (nm)	17.8	21.1	18.4

since a single STZ (~ 1 nm) that has accumulated extreme shear strain and bonding distortion could initiate internal decohesion (irreversible loss of total metal–metal coordination, TMMC) that may lead to the final catastrophic failure of the entire sample. In fact, Murali et al. have recently identified a characteristic spatial correlation ~1 nm of plastic displacement that may be responsible for the fracture mode in MGs [46]. Here, we collected EV statistics by plotting the histogram of von Mises strain after 6% applied strain to different finite-sized $\mathbf{IC}_1$ samples, shown in Fig. 9, where those long tails contains EVs of interest. (Here EV refers to a net von Mises strain exceeding 0.2, which is twice the characteristic shear of a STZ.) It is shown that when subjected to the same macroscopic strain, the bulk sample experiences much more intense EVs than finite-sized samples, as indicated by a longer tail in Fig. 9. Smaller samples, on the other hand, tend to have more moderate EVs, and thus are more failure resistant.

4.4. Intersections of shear bands

Apart from EVs, it would be beneficial to know where those extreme sites (sites with EVs) are actually located in the deformed samples. For the bulk, EVs should occur within the dominant shear band, and the center of the shear band experiences the most severe plastic deformation [13]. This can be seen in Fig. 8, which also resembles the thermal profile of a shear band [47]. Since a shear band is approximately a planar defect, those extreme sites are likely to be distributed uniformly in the shear plane, which is confirmed in our simulations. These extreme sites sustain the largest bond reconfigurations, have the highest local temperature, and are most susceptible to loss of TMMC and initiation of cavitation under even a small local tensile stress, which leads to the final catastrophic failure along the dominant shear band plane.

What if there are multiple shear bands? Do we still expect extreme sites to be uniformly distributed within each band? The line of intersection between two shear bands is a likely location of EV concentration and could be significant for predicting subsequent failure processes. In Fig. 7(c) we see that two shear bands nucleate one after the other and intersect with each other. To inspect the corresponding EV distribution, we increase the plotting threshold value in Fig. 7(c) to 0.23 in strain, which contains the full EV tail in Fig. 9. The new contour plot is shown in Fig. 10. It is now clear that extreme sites are localized in the intersection region of the two shear bands. This gives rise to a 1-D (line) "weak" region, which could be a major source of cavitation [48]. While we have not seen it yet in our kMC simulations, it is geometrically possible for three shear bands to intersect at a point. We speculate that these 0-D "triple points" could harbor the most extreme sites for damage and cavitation.

4.5. Surface contamination: size effect

Because of surface contamination, extended defects can be initiated either near surfaces ($\mathbf{IC}_3$, surface softening) or within the interior ($\mathbf{IC}_4$, surface hardening). It is then expected that the fraction of the surface STZs could influence the actual strengths directly, giving another possible size effect. Consider $\mathbf{IC}_3$: STZs near surfaces will be activated earlier than those in the interior. If the fraction of surface STZs is relatively small, the majority of material will not yield until the sample is stressed up to a level approaching the strength of the interior, i.e. $\mathbf{IC}_1$. As the sample size decreases, the fraction of the surface STZs will

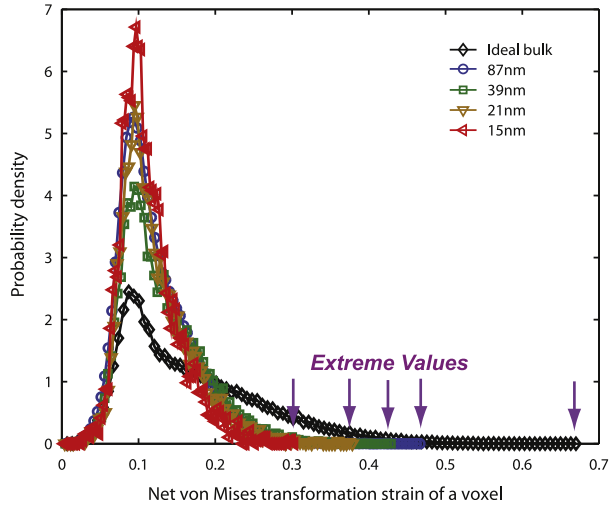

Fig. 9. Probability density distributions of von Mises strain of voxels after 6% applied strain in samples of Fig. 5(a).

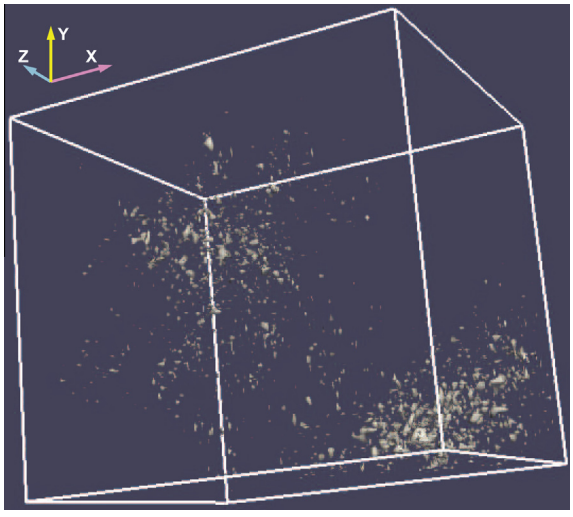

Fig. 10. Same as Fig. 7(c) but with a strain threshold of 0.23.

increase. At certain point, the yielding of surface layers, which now possess a considerable volume fraction, will result in a global stress relaxation.

Similar analysis also holds for the surface hardening case. Note that the apparent strain hardening shown by the stress–strain curves (Fig. 5(d)) of $\mathbf{IC}_4$ samples smaller than or equal to 27 nm is due to the elastoplastic transition. Once this transition is over, the stress decreases in an overall sense as the deformation continues. This is consistent with our expectation, as there is no intrinsic hardening mechanism for the constitutive behavior of STZ in our model. The apparent strain hardening is due to two-stage deployment of bulk and then surface STZs before the former soften too much. Eventually, as both populations are deployed and soften, the overall response switches to softening.

Fig. 11 plots the peak stress in Fig. 5(c) and (d) against the inverse of sample sizes, showing that smaller can be either "stronger" or "weaker". For large $\mathbf{IC}_3$ samples, the "weak" region (i.e. the surface layer) possesses a small volume fraction. This is actually similar to small $\mathbf{IC}_4$ samples, where the "weak" region now becomes the interior. As $\mathbf{IC}_3$ samples decrease in size or $\mathbf{IC}_4$ samples increase in size, the volume fraction of the "weak" region will increase. This may explain the similar slope changes in the two curves in Fig. 11 (from left to right in $\mathbf{IC}_3$ and from right to left in $\mathbf{IC}_4$).

4.6. Connected-free-volume analysis and strengths of MGs

In Section 2.2 we have introduced two concepts, reference glass and CAFV spectrum. The reference glass is defined to have a finite but limited tail in the CAFV spectrum, which is nearly impossible to extend beyond a critical value (e.g. tens of atomic volume). Any CAFV that goes beyond this is not "intrinsic" heterogeneity of the reference glass, and is identified as an extended defect. We hypothesize that extended defects can only be created in the presence of external mechanical-chemical driving forces such as FIB, corrosion, shear bands due to previous mechanical service, or high-energy radiation. Here we want to illustrate

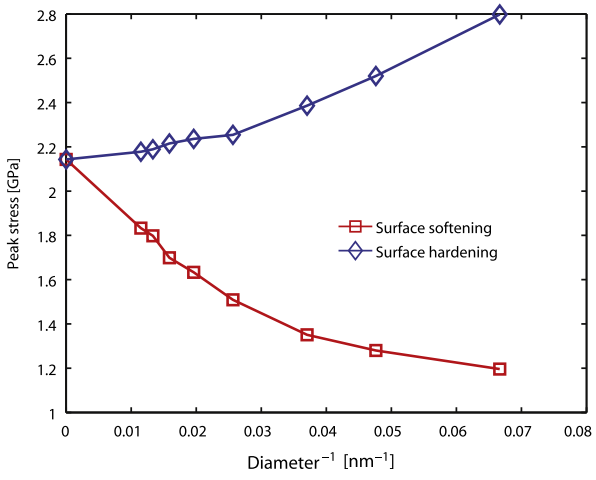

Fig. 11. The peak stress from Fig. 5(c) and (d) plotted against the inverse of sample sizes.

these concepts with our kMC simulations. Because STZ modeling is coarse-grained over atomistics, we do not have atomistic free volume (AFV) information. However, we may consider a similar "connected free volume" (CFV) concept, which is the voxel-level free volume represented by the degree of softening in each voxel. CFV examines the topological connectivity of voxels with a large degree of softening and essentially represents the volume of an extended defect, times 1% which is the volume dilation in a shear band (free volume) estimated from atomistic simulation [39] and experiments [21]. Previous plots of Figs. 4 and 7 should already give us some hints of how the CFV spectrum evolved over time, but below we show this evolution more explicitly.

In Fig. 12 we plot the von Mises strain distributions immediately before (left column), at (middle column) and after (right column) the peak stress for 87 nm (top row) and 21 nm (bottom row) $\mathbf{IC}_1$ samples. Before the peak stress, STZs are only activated locally. When σ_{peak} is reached, local STZ clusters start to connect to each other and span across the whole sample, giving rise to a "sample-spanning cluster" (a peak at the far right of the CAFV spectrum) and resulting in a global instability. While we expect that in larger samples a more explosive growth of the spanning cluster should follow (see discussion about Fig. 7 in Section 3), σ_{peak} in $\mathbf{IC}_1$ samples is more likely to be related to factors such as the microelastic interaction between STZs and temperature, and be hence insensitive to sample size, as shown in Fig. 5(a).

In the "more realistic" $\mathbf{IC}_2$ samples, extended defects may or may not be nucleated, depending on the amount of pre-straining. Consequently, the actual strength should also depend on the amount of pre-strain. Fig. 13 shows the relation between the peak stress and the amount of pre-strain for a given finite-sized $\mathbf{IC}_2$ sample. Obviously, there is a sharp change in the peak stress when the sample is pre-strained above 0.025, which is close to the yield point of $\mathbf{IC}_1$ sample. (Experiments by Bei et al. have also revealed a similar relationship between the yield strength and pre-strain in crystals [49].) Since the $\mathbf{IC}_2$ in Table 1 specifies a pre-strain of 0.03, some extended defects are very likely to be formed during pre-straining. The difference now is the percolation level of those pre-formed extended defects, which should be related closely to the sample size. To understand the size-dependent strength results (Fig. 6), quantitative representations of the initial $\mathbf{IC}_2$ samples are required. Here we perform connectivity analysis on the binarized von Mises strain distributions using a threshold of 0.05 (half of the characteristic shear of STZ) and obtain the CFV, which is measured by the voxel volume of the identified connected clusters in the obtained binary "image", times 1% which is an estimated dilation (density change) in mature shear band from atomistic simulation [39] and experiments [21]. Fig. 14 plots the results for three $\mathbf{IC}_2$ samples with different sizes. (Note that the peak corresponding to the reference glass in the CAFV spectrum is now reduced to a delta-function peak at CFV = 0 and is not included in the plot.) The initial CFV spectra shown

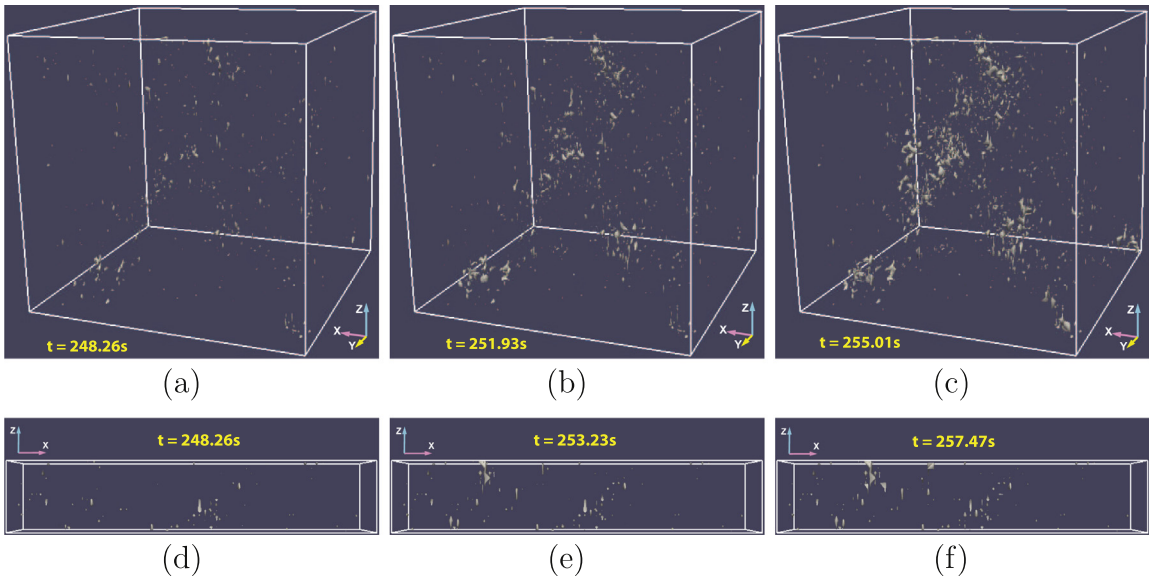

Fig. 12. Von Mises strain distributions plotted in contour representation immediately before (left column), at (middle column) and after (right column) peak stress, for $\mathbf{IC}_1$ samples with cross-section of 87 nm × 87 nm (top row) and 21 nm × 21 nm (bottom row). The strain threshold is 0.1. The real times from kMC are also indicated.

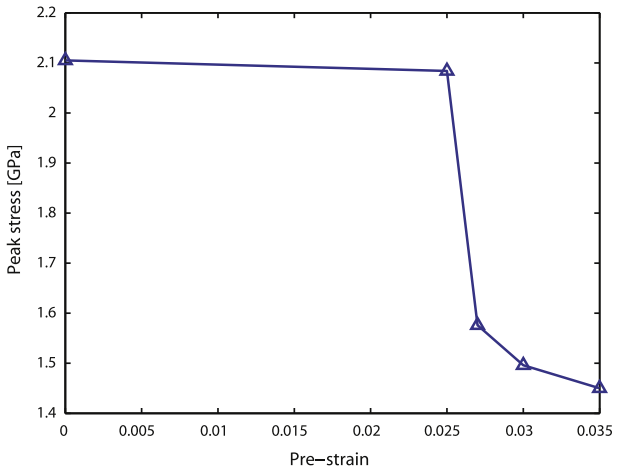

Fig. 13. Peak stress vs. amount of pre-loading strain for a given finite-sized sample with a 51 nm × 51 nm cross-section.

in Fig. 14(a) indicate clearly that under the same initial treatment, i.e. pre-straining and relaxation, larger samples tend to build up much longer CFV tails than smaller ones. After the samples have undergone 3% elongation, the largest CFV in all samples show explosive growth (one order of magnitude increase) as shown in Fig. 14(b), suggesting the evolution of CFV $\rightarrow \infty$ post peak-stress.

Fig. 14 directly illustrates the central concept of this paper, namely that extended defects are fundamentally different and thus distinguishable from intrinsic heterogeneities in the glass, based on their CFV's raw magnitude and tendency for runaway growth under uniform applied stress, so much so that the horizontal axis of Fig. 14(b) has to be plotted on a log-scale. The largest-CFV defect can even dominate the deformation of the entire sample, and directly cause its catastrophic failure. By this token, the size effect on strength is closely tied to the specification of the initial condition, i.e. what the CFV/CAFV spectrum looks like before external stress is applied. In this regard, i.e., an intimate relationship exists between size effect and initial condition sensitivity, MGs are no different from crystals [6].

4.7. Statistical treatment and data sampling

Apart from the more fundamental limitations and approximations of our method, we also have some pragmatic issues. In principle, we should show ensemble-averaged results in addition to individual trajectories. That is, we should perform simulations and analysis on an ensemble of initial conditions with the same statistical specification, but drawing different instances using different pseudo-random number generator seeds. In the current study a single simulation trajectory is carried out for each case considered. In principle, multiple simulations should be carried out for each case with the same IC but different seeds for the random number generator used in the kMC algorithm, and then report the average value of the peak stress with an error bar. However, this is time consuming at the moment and has not been done. Nevertheless, the qualitative nature of the results and the conclusions from the study should remain largely the same.

It also needs to be pointed out that, since we focus on the spatial percolation during shear localization, the time interval we used in analyzing yielding (Fig. 12) is ~ 3 s, which is much larger than the suggested time of shear band nucleation based on another STZ dynamics modeling [50] and MD simulations [39,40]. As a result, if the very initial stage of shear localization is to be studied, we need to

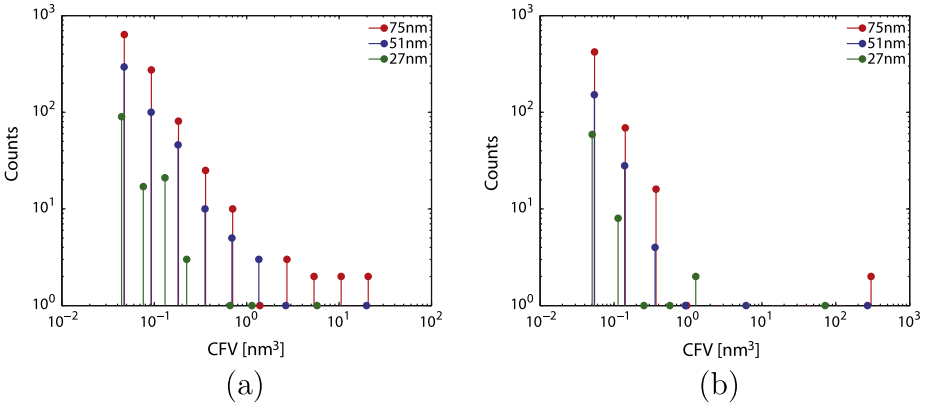

Fig. 14. "Connected free volume" (CFV) analysis on three $\mathbf{IC}_2$ samples at (a) initial and (b) 3% applied strain stages.

record the consecutive strain distributions at a much higher time-sampling frequency during the simulations.

5. Conclusions

Based on the proposed CAFV concept that characterizes the extent of percolation of free volume in MGs, we define the perfect or reference glass, upon which the ideal strength of glass is defined through the forced percolation of atomistic free volume. The laboratory-made samples differ from the reference glass by the so-called "extended defects" that are above and beyond inherent atomic heterogeneities. The stochastic behavior of the experimentally measured strengths is explained using a simple stochastic model.

Different ICs are designed to simulate the starting microstructure of different MG samples. In particular, samples (i) free of extended defects and residual stresses, (ii) with damage and residual stress introduced by a "pre-straining and relaxation", and containing (iii) softened or (iv) hardened STZs at surface layers, are produced to perform tensile test simulations using a kMC STZ dynamics model. Results show that the ideal MGs exhibit the same "ideal" strength regardless of their sizes. "Smaller is stronger" is observed in samples that initially contain extended defects introduced by pre-straining. The CFV, analogous to CAFV on the STZ scale, is analyzed to show that under the same initial treatment larger samples tend to build up larger CFVs than smaller ones. Samples with "contaminated" surface layers exhibit either "smaller is weaker" or "smaller is stronger", depending on whether the surface STZs are softer or harder than the bulk STZs.

Simulations also reveal a deformation mode transition as finite-sized samples shrink down to a scale comparable to the shear band thickness w, which is ~ 20 nm in our simulations. It is found that when samples are much larger than w, plastic deformation occurs through the formation of well-defined shear bands of large aspect ratios and the shear bands of different orientations intersect with each other. When the sample size becomes $\sim w$. However, equiaxed and spatially independent shear bands are formed. Extreme value statistics reveals that smaller samples are inherently more damage-tolerant, and the intersection of two shear bands is where the materials experience the most severe plastic shear and are prone to extreme bonding distortions and subsequent cavitation.

A glaring deficiency of the current STZ-level simulations is that $\mathbf{IC}_1$ (which $\mathbf{IC}_2$ starts off with), $\mathbf{IC}_3$ and $\mathbf{IC}_4$ all have zero STZ-level residual stresses, whereas MD simulations have shown that atomistic residual stresses in the reference MG state in both shear and hydrostatic components [25] could be very significant even before deformation. $\mathbf{IC}_2$ does have STZ-level residual stresses, which is, however, all deformation generated and lacks the "intrinsic" contribution inherited from cooling the liquid. At the end of Ref. [13] we have discussed how a self-balancing STZ-level residual stress field could be generated as part of the initial condition, but we have not yet analyzed such as stress field in this paper. While we aim to link our STZ-level simulations to atomistic simulations, we are also hampered by the fact that current MD simulations still lack the timescale reach (the MD cooling rate is too high compared to the experimental cooling rate) to generate the "reference glass" or "perfect glass" state. As a result, the residual stress distribution obtained with MD simulations may not yet closely represent the reference glass state obtained with the experimentally accessible cooling rate from the liquid. Because of this timescale challenge, the reference glass state with the experimental cooling rate is conceptually well defined, but numerically unobtainable today with MD. For this reason, we have limited our STZ-level simulations to parametric studies in this paper. In the future, accelerated timescale atomistic simulations should allow us to obtain or approach the reference glass state with the experimental cooling rate. This would then allow us to compute the ideal strength atomistically, as well as giving a more realistic starting point for carrying out STZ-level kMC simulations.

Acknowledgements

We acknowledge supports by NSF under Grants DMR-1120901 (J.L.), DMR-1008349 (P.Z. and Y.W.),

NSF DMR-1240933 and by AFOSR under Grant FA9550-09-1-0014 (Y.W.). Computational time on the Extreme Science and Engineering Discovery Environment (XSEDE) under Grant No. TG-DMR130038 is gratefully acknowledged.

Appendix A. Randomized event catalogs for 3-D STZ

The randomized event catalog for a STZ, where the glass nature resides in a mesoscale model, is the key ingredient. More specifically the isotropy of glass structures suggests that the overall transformations of each voxel should also be statistically isotropic. We first write the SFTS tensor for a 3-D STZ in the following form:

$$\epsilon = \begin{pmatrix} \epsilon_1 & \epsilon_6 & \epsilon_5 \\ \epsilon_6 & \epsilon_2 & \epsilon_4 \\ \epsilon_5 & \epsilon_4 & \epsilon_3 \end{pmatrix}, \tag{A.1}$$

with the constraint $\mathrm{Tr}(\boldsymbol{\epsilon}) = \epsilon_1 + \epsilon_2 + \epsilon_3 \equiv 0$, implying that the plasticity is assumed to be shear-dominant and the volume change is thus ignored. To represent the inherent structural isotropy of MGs, we numerically generate $\boldsymbol{\varepsilon}$ such that

$$\tilde{\boldsymbol{\epsilon}} = \mathbf{R}^T \boldsymbol{\epsilon} \mathbf{R}, \tag{A.2}$$

where $\mathbf{R}$ is an arbitrary rotation matrix. The rotational invariance can be verified by plotting the empirical cumulative distribution function and the histogram for any generated component of $\boldsymbol{\epsilon}$ in original and rotated frames. In Fig. A.15 the component ϵ_{13} is shown as an example to verify the preserved isotropy under arbitrary rotation.

Appendix B. Inhomogeneous elasticity solver

From our previous work [13], the stress equilibrium equation for a structurally and elastically inhomogeneous system is:

$$\left(c_{ijpq}(\mathbf{x})(u_{p,q}(\mathbf{x}) - \epsilon_{pq}(\mathbf{x}))\right)_{,j} = 0, \quad \forall\, i = 1, \ldots, 3 \tag{B.1}$$

where $c_{ijpq}(\mathbf{x})$ are the spatially varied elastic constants, $u_p(\mathbf{x})$ is the displacement field, and $\epsilon_{pq}(\mathbf{x})$ is the SFTS tensors field. In Ref. [13] we solve Eq. (B.1) for an elastically homogeneous system, i.e. $c_{ijpq}(\mathbf{x}) \equiv c_{ijpq}$. For issues such as cavitation and free surface, one has to consider the elastic inhomogeneity.

To solve Eq. (B.1) for a general case, we borrow the idea from Ref. [18] that by introducing an appropriate reference homogeneous system c°_{ijpq}, solving the original inhomogeneous system becomes equivalent to solving this reference homogeneous system. In other words, we can always tune the virtual SFTS field $\epsilon^\circ_{pq}(\mathbf{x})$ of the reference homogeneous system such that:

$$c_{ijpq}(\mathbf{x})(u_{p,q}(\mathbf{x}) - \epsilon_{pq}(\mathbf{x})) = c^\circ_{ijpq}(u_{p,q}(\mathbf{x}) - \epsilon^\circ_{pq}(\mathbf{x})). \tag{B.2}$$

Since there are as many equations (stress components) as unknowns (SFTS components that do not need to satisfy compatibility [51]), Eq. (B.2) has a unique solution for positive definite c°_{ijpq}. Thus there is a one-to-one mapping between a given inhomogeneous system and a virtual homogeneous system, and vice versa. Then suppose we know what $\boldsymbol{\epsilon}^\circ(\mathbf{x})$ should be used, it is easy to obtain the displacement field, total strain field and stress field following Ref. [13], i.e.

$$\boldsymbol{\epsilon}^\circ(\mathbf{x}) \rightarrow \mathbf{u}(\mathbf{x}), \quad \boldsymbol{\epsilon}(\mathbf{x}), \quad \boldsymbol{\sigma}(\mathbf{x}). \tag{B.3}$$

The above-obtained fields should be identical to those of the original inhomogeneous system, and thus satisfy Eq. (B.2), or equivalently:

$$c^\circ_{ijpq}\epsilon^\circ_{pq}(\mathbf{x}) = c_{ijpq}(\mathbf{x})\epsilon_{pq}(\mathbf{x}) + (c^\circ_{ijpq} - c_{ijpq}(\mathbf{x}))\epsilon_{pq}(\mathbf{x}), \tag{B.4}$$

where the symmetry of elastic constants has been employed. If, however, the initial guess of $\boldsymbol{\epsilon}^\circ(\mathbf{x})$ is not exact, Eq. (B.4) will not be satisfied. In this case, we can simply invert the right-hand side to update the estimate $\boldsymbol{\epsilon}^\circ(\mathbf{x})$, and repeat the process until convergence is reached. As long as the system is not significantly far from an elastically homogeneous state, the inhomogeneity can be regarded as a perturbation and convergence should be fast. As a result, our previous Fourier space solver for homogeneous systems can be easily adapted to solve the current inhomogeneous system by iteration.

We test our solver by considering a spherical void in an infinite, isotropic linear elastic solid subjected to a tensile stress $\sigma_{zz} = \sigma^\infty_{zz}$, with all other far-field stress components being zero. There exists an analytical solution [52] for this problem and the comparison with our simulation result is shown in Fig. B.16. To speed up the iteration, the so-called "raised cosine filter" can also be employed to filter out high-frequency waves. In Fig. B.16 the "filtered Fourier" results correspond to calculations with the filter being used, and it takes only 242 steps to achieve the same level of

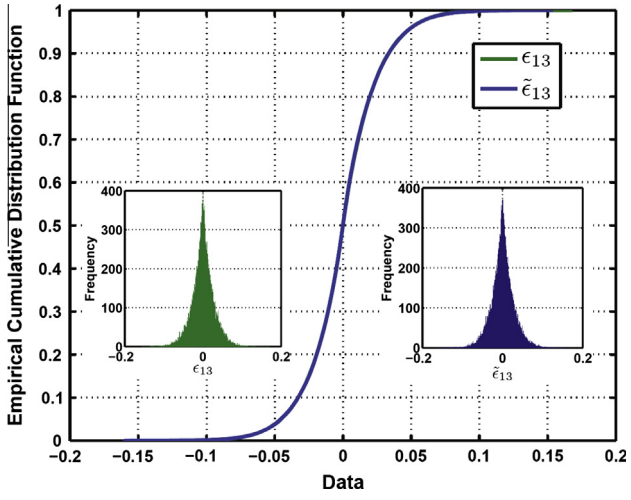

Fig. A.15. The empirical cumulative distribution function of strain component ϵ_{13} and $\tilde{\epsilon}_{13}$ in the original and rotated frames, respectively. Note that the two curves almost perfectly coincide with each other. The insets are the corresponding histograms.

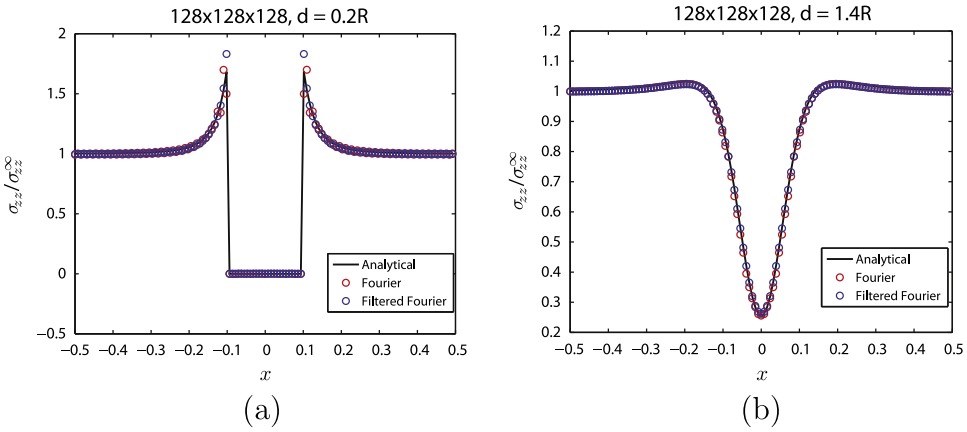

Fig. B.16. The σ_{zz} component of the stress field along a line (a) going through and (b) outside the spherical void. d corresponds the distance between the center of the void and the lines, which are both parallel to the x-axis.

relative precision which would take 5000 steps for calculations without using the filter.

References

[1] Hull D, Bacon DJ. Introduction to dislocations. Butterworth-Heinemann; 2001.
[2] Zhu T, Li J. Prog Mater Sci 2010;55:710.
[3] Johnson W, Samwer K. Phys Rev Lett 2005;95:195501.
[4] Tian L, Cheng YQ, Shan ZW, Li J, Wang CC, Han XD, et al. Nat Commun 2012;3:609.
[5] Wang C, Ding J, Cheng Y, Wan J, Tian L, Sun J, et al. Acta Mater 2012;60:5370.
[6] Wang ZJ, Shan ZW, Li J, Sun J, Ma E. Acta Mater 2012;60:1368.
[7] Cheng Y, Ma E. Acta Mater 2011:59.
[8] Greer J, DeHosson J. Prog Mater Sci 2011;56:654.
[9] Liu Y, Zhao F, Li Y, Chen M. J Appl Phys 2012;112:063504.
[10] Bulatov V, Argon A. Model Simul Mater Sci Eng 1994;2:167.
[11] Homer E, Schuh C. Acta Mater 2009;57:2823.
[12] Ogata S, Shimizu F, Li J, Wakeda M, Shibutani Y. Intermetallics 2006;14:1033.
[13] Zhao P, Li J, Wang Y. Int J Plasticity 2013;40:1.
[14] Eshelby J. Proc Roy Soc Lond Ser A – Math 1957;241:376.
[15] Li L, Homer E, Schuh C. Acta Mater 2013.
[16] Yu H, Wang W, Bai H, Wu Y, Chen M. Phys Rev B 2010;81:220201.
[17] Rodney D, Schuh C. Phys Rev Lett 2009;102:235503.
[18] Wang Yu U, Jin Y, Khachaturyan A. J Appl Phys 2002;92:1351.
[19] Stukowski A, Bulatov VV, Arsenlis A. Model Simul Mater Sci Eng 2012;20:085007.
[20] Flores KM, Suh D, Dauskardt RH, Asoka-Kumar P, Sterne PA, Howell RH. J Mater Res 2002;17:1153.
[21] Li J, Spaepen F, Hufnagel TC. Philos Mag A – Phys Condens Matter Struct Defect Mech Prop 2002;82:2623.
[22] Wang CC, Mao YW, Shan ZW, Dao M, Li J, Sun J, et al. Proc Natl Acad Sci USA 2013;110:19725.
[23] Pekarskaya E, Kim C, Johnson W. J Mater Res 2001;16:2513.
[24] Stillinger FH. Phys Rev E 1999;59:48.
[25] Srolovitz D, Maeda K, Vitek V, Egami T. Philos Mag A 1981;44:847.
[26] Li J, Ngan AHW, Gumbsch P. Acta Mater 2003;51:5711.
[27] Morris JR, Bei H, Pharr GM, George EP. Phys Rev Lett 2011;106:165502.
[28] Mayr S. Phys Rev Lett 2006;97:195501.
[29] Pan D, Inoue A, Sakurai T, Chen M. Proc Natl Acad Sci USA 2008;105:14769.
[30] Roduner E. Chem Soc Rev 2006;35:583.
[31] Delogu F. Phys Rev B 2009;79:184109.
[32] Shim S, Bei H, Miller M, Pharr G, George E. Acta Mater 2009;57:503.
[33] Bei H, Shim S, Miller M, Pharr G, George E. Appl Phys Lett 2007;91:111915.
[34] Chen DZ, Jang D, Guan KM, An Q, Goddard WA, Greer JR. Nano Lett 2013;13:4462.
[35] Bian Z, Pan M, Zhang Y, Wang W. Appl Phys Lett 2002;81:4739.
[36] Dubach A, Torre FD, Löffler J. Philos Mag Lett 2007;87:695.
[37] Argon A, Shi L. Acta Metall 1983;31:499.
[38] Schuh C, Hufnagel T, Ramamurty U. Acta Mater 2007;55:4067.
[39] Shimizu F, Ogata S, Li J. Acta Mater 2006;54:4293.
[40] Shimizu F, Ogata S, Li J. Mater Trans 2007;48:2923.
[41] Lu J, Ravichandran G, Johnson WL. Acta Mater 2003;51:3429.
[42] Zhang Y, Greer A. Appl Phys Lett 2006;89:071907.
[43] Reiss RD, Thomas M. Statistical analysis of extreme values: with applications to insurance, finance, hydrology and other fields. Birkhauser Basel 2007.
[44] Jang D, Greer J. Nat Mater 2010;9:215.
[45] Kim JY, Jang D, Greer JR. Adv Funct Mater 2011;21:4550.
[46] Murali P, Zhang Y, Gao H. Appl Phys Lett 2012;100:201901.
[47] Lewandowski J, Greer A. Nat Mater 2005;5:15.
[48] Greer A, Cheng Y, Ma E. Mater Sci Eng R: Rep 2013;74:71.
[49] Bei H, Shim S, Pharr GM, George EP. Acta Mater 2008;56:4762.
[50] Homer ER. Acta Mater 2014;63:44.
[51] Mura T. Micromechanics of defects in solids. Second rev. ed. Kluwer Academic Publishers; 1991.
[52] Lee H, Ju J. Int J Damage Mech 2007;16:331.